

## SPECIAL ISSUE ARTICLE

# Dislocation-induced local symmetry reduction in single-crystal $\text{KNbO}_3$ observed by Raman spectroscopy

Felix Drechsler<sup>1</sup>  | Cameliu Himcinschi<sup>1</sup>  | Oliver Preuß<sup>2</sup> | Xufei Fang<sup>3</sup>  | Jens Kortus<sup>1</sup> 

<sup>1</sup>TU Bergakademie Freiberg, Institute of Theoretical Physics, Freiberg, Germany

<sup>2</sup>Department of Materials and Earth Sciences, Division Nonmetallic-Inorganic Materials (NAW) TU Darmstadt, Darmstadt, Germany

<sup>3</sup>Karlsruhe Institute of Technology, Institute for Applied Materials, Karlsruhe, Germany

## Correspondence

Felix Drechsler, TU Bergakademie Freiberg, Institute of Theoretical Physics, D-09596 Freiberg, Germany.

Email:

[Felix.Drechsler@physik.tu-freiberg.de](mailto:Felix.Drechsler@physik.tu-freiberg.de)

## Funding information

Deutsche Forschungsgemeinschaft, Grant/Award Numbers: 461482547, 414179371; European Research Council, Grant/Award Number: 101076167

## Abstract

In recent years, dislocation-tuned functionalized ceramics have become one of the focal points of modern materials research due to their outstanding properties. These range from improved electrical conductivity and ferroelectric properties to dislocation-enhanced toughening and superconductivity, caused by local strain fields. The aim of this work is to investigate the dislocation-induced structural changes in single-crystal  $\text{KNbO}_3$  by micro-Raman spectroscopy. Dislocation-rich regions with tailored densities have been generated using the Brinell indenter scratching method. The influence of the dislocations on the single-crystal structure can be observed in the Raman spectra. The activation of additional Raman modes is observed, which does not occur in regions of low dislocation density. This observation is confirmed by DFT calculations of vibrational modes and is attributed to a reduction in the crystal symmetry due to increased defect densities in plastically deformed  $\text{KNbO}_3$ . In addition, an increase in compressive stress at higher dislocation densities can be demonstrated by a blueshift in Raman mode positions.

## KEYWORDS

dislocations,  $\text{KNbO}_3$ , Raman spectroscopy, single crystal

## 1 | INTRODUCTION

Ceramic ferroelectric materials are essential to modern microelectronics. They offer a wide range of applications, such as in sensors, in capacitors, in data storage or for energy harvesting.<sup>1–3</sup> For these applications, it is important to control the electronic properties of such materials. To achieve this, crystal defects have been shown to be a powerful tool. The introduction of point defects by doping is one of the most studied area of defect engineering and has wide

industrial application.<sup>4–6</sup> The use of higher dimensional defects such as dislocations is not yet well established as ceramics have long been considered dislocation-free and dislocation generation by plastic deformation at room temperature (RT), as is known from metallic materials, was considered impossible due to their brittle behavior.

However, recent studies have shown that some ceramics exhibit a high degree of plastic deformability even at RT, which was an unexpected result.<sup>7–11</sup> This opened up the new and promising field of dislocation-tuned

This is an open access article under the terms of the [Creative Commons Attribution](https://creativecommons.org/licenses/by/4.0/) License, which permits use, distribution and reproduction in any medium, provided the original work is properly cited.

© 2024 The Author(s). *Journal of the American Ceramic Society* published by Wiley Periodicals LLC on behalf of American Ceramic Society.

ceramic materials. Various techniques have been developed to generate dislocations in ceramics, for example by mechanical imprinting with a Brinell indenter.<sup>12–14</sup> This approach is not only easy to apply, but is also able to generate tailored dislocation densities.<sup>10,12,15</sup> These advances are driving the development of dislocation-functionalised ceramics. There is great interest in these materials as recent studies have shown their potential for applications and their outstanding mechanical and physical properties: dislocation-tuned ferroelectric ceramics show a reduction in thermal conductivity,<sup>16</sup> improvements in local electrical conductivity<sup>17</sup> and fracture toughness,<sup>15,18</sup> and an increase in coercivity due to domain wall pinning.<sup>19–21</sup> Even though the plastic deformation of ceramics has already been successfully demonstrated experimentally, the fundamental mechanisms behind it have not yet been sufficiently clarified. It is not yet possible to control the dislocation plasticity of ceramics, and it is still unclear why some ceramics exhibit good plastic deformation and others do not although they have the identical crystal structure.<sup>14</sup> One piece of the puzzle is the structural elucidation of the dislocations. Raman spectroscopy could be a suitable method to clarify these aspects. This technique is very sensitive to the lattice dynamics and can detect slight changes in the crystal structure and the crystal symmetry. It is already used successfully as a method for the study of phase transitions,<sup>22–25</sup> crystal strain,<sup>26–28</sup> and domain structures.<sup>29,30</sup> Therefore, it has great potential for the structural investigation of dislocations. This has already been demonstrated for various materials such as semiconductors<sup>31–33</sup> or different oxides.<sup>34,35</sup> Despite that dislocations in perovskite ceramics is a topic that has gained more and more importance in recent years, there are limited Raman investigations.<sup>36,37</sup> However, Raman spectroscopy can contribute to the understanding of dislocation dynamics, which is our intention in this work to conduct a comprehensive Raman study on dislocations in  $\text{KNbO}_3$ .

In this work, we investigate perovskite single-crystal potassium niobate ( $\text{KNbO}_3$ ) with mechanically imprinted dislocation-rich regions by Raman spectroscopy. We are concerned with the question of which structural changes in the crystal lattice are caused by dislocations and have therefore divided our investigations into two parts. First, we focused on the pristine, dislocation-scarce areas of the single-crystal sample, which serve as a reference. Second, the dislocation-rich areas of different dislocation density were analyzed and compared with the pristine single crystal to determine changes in the Raman spectra and thus in the crystalline structure. This interpretation is further supported by the density functional theory (DFT) calculations of Raman modes.

## 2 | MATERIAL AND METHODS

### 2.1 | Single-crystal material and dislocation imprinting

Undoped bulk single-crystal  $\text{KNbO}_3$  with stripe-like ferroelastic domains (see Figure S4a) prepared by top-seeded solution growth (FEE GmbH, a division of EOT, Idar-Oberstein, Germany) with orthorhombic structure  $Amm2$  at RT was used for our investigations. The sample material was cut in ( $4 \times 4 \times 1.5$ ) mm dimensions with  $\langle 110 \rangle$  pseudo-cubic directions parallel to the edges. For dislocation imprinting, the cyclic Brinell indenter scratching method<sup>12</sup> was applied at RT using a universal hardness testing machine (Finotest, Karl-Frank GmbH, Weinheim-Birkenau, Germany) mounted with a hardened steel Brinell indenter of 2.5 mm diameter. The Brinell indenter scratched on the (100) surface along a  $\langle 110 \rangle$  direction with a load of 7.85 N (0.8 kgf) and a velocity of  $0.5 \text{ mm s}^{-1}$ , controlled by a moving single-axis piezo stage (PI Instruments, Karlsruhe, Germany). Silicone oil was used as a lubricant during the scratch tests. The plastically deformed scratch tracks have a width of 150  $\mu\text{m}$  and extend over a length of several millimetres.

### 2.2 | Dislocation and Brinell zone imaging

The plastically deformed scratch tracks were visualized by the polarized optical microscopy. These light microscopic investigations were performed on a Zeiss Axio Imager A1 m (Oberkochen, Germany) with a 10 $\times$  EC Epiplan-Neofluar objective and switched-on prism for Nomarski Differential Interference Contrast (Nomarski DIC) microscopy.<sup>38</sup>

Further characterization was done by electron channeling contrast imaging (ECCI)<sup>39</sup> within a Tescan MIRA3-XM (Tescan, Brno, Czech Republic) equipped with a four-quadrant solid-state BSE detector (DEBEN, Woolpit, UK) was used. The acceleration voltage was 15 kV, the working distance 8 mm. As  $\text{KNbO}_3$  is an isolator, a carbon layer of approximately 10 nm thickness was sputtered on top of the ECCI sample (EmiTech K950X sputter coater, Emitech, Saint-Quentin-en-Yvelines, France).

### 2.3 | Raman scattering measurements

Micro-Raman scattering measurements were performed on Horiba LabRam System-HR-800 spectrometer (Villeneuve d'Ascq, France) (1800 lines  $\text{mm}^{-1}$  grating, charge-

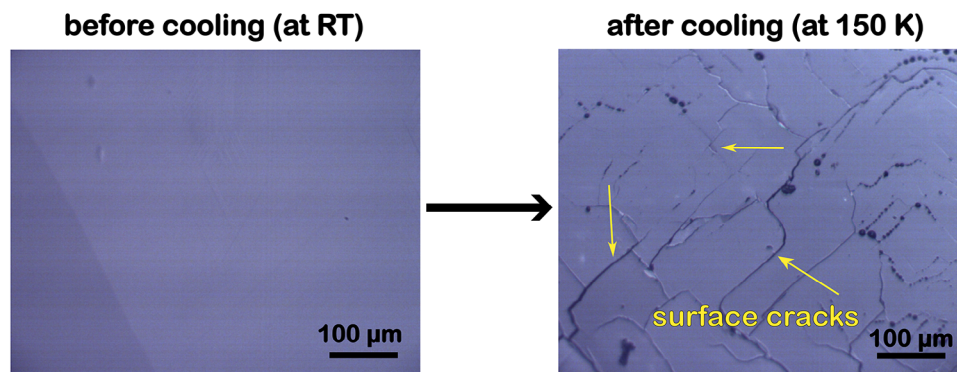


**FIGURE 1** Optical microscope image of the  $\text{KNbO}_3$  sample at RT before cooling and at 150 K after cooling. The high cooling rate of  $2 \text{ K min}^{-1}$  resulted in thermal stresses which led to the formation of surface cracks. These did not penetrate through the entire thickness of the material as the bulk sample did not break into pieces. RT, Room temperature.

coupled device camera) in the backscattering geometry using the 442 nm excitation line of a He–Cd laser. The laser power was set to 1.3 mW, which gave sufficiently high measurement intensities and did not induce sample heating. The laser beam was focused on the sample surface by a  $50\times$  magnification objective (N. A. 0.55) and had a spot size of  $\sim 1 \mu\text{m}$ . Due to the optical transparency of  $\text{KNbO}_3$ ,<sup>40</sup> the excitation volume is not limited by the penetration depth, but by the depth of focus, which is  $\sim 8 \mu\text{m}$ .

Raman measurements of the dislocation-rich plastic zones were carried out at RT. Additionally, we performed temperature-dependent Raman measurements from 150 to 525 K, which were carried out in a Linkham THMS-600 temperature control stage (Salfords Redhill, UK) placed under the Raman microscope. The sample was fixed with a temperature resistant silver paste, which also improves heat transfer. The cooling and heating rates were set at  $2 \text{ K min}^{-1}$ . It should be mentioned that the Raman investigations of the Brinell zones were performed before the cooling/heating process. After cooling the sample to 150 K, surface cracks could be observed under an optical microscope, as shown in Figure 1. Therefore, the regions of interest for the temperature-dependent Raman measurements in the pristine sample areas were carefully chosen to be away from the cracks to avoid any potential influence on the Raman spectra.

We used the Python-based open-source graphical user interface PyRamanGUI<sup>41</sup> for spectra evaluation.

## 2.4 | Raman spectrum calculation

All DFT calculations<sup>42,43</sup> were performed using the Quantum Espresso code<sup>44–46</sup> version 6.8 together with projector augmented-wave (PAW) pseudopotentials<sup>47</sup> taken from the PSLibrary, version 1.0.0.<sup>48</sup> The PAW pseudopotentials were combined with the Perdew–Burke–Ernzerhof generalized-

gradient exchange–correlation functional.<sup>49</sup> The calculations have been carried out with a kinetic energy cutoff of 80 Rydberg, whereas the density cutoff has been 8 times larger. In case of the Brillouin zone integration, a  $14 \times 10 \times 10$  mesh in reciprocal space has been employed. The calculation focuses on the orthorhombic structure which is observed at RT in experiment. Starting from the experimental orthorhombic crystal structure obtained from ICSD (database code #37219) the nuclear positions and the cell parameters have been relaxed until the nuclear forces were  $<0.1 \text{ mRy Bohr}^{-1}$  and cell pressure  $<0.1 \text{ kbar}$ . The Raman spectra have been calculated using the phonon code, which is part of Quantum Espresso using only the Gamma point. The method is based on the linear response theory and makes use of symmetry if available.

## 3 | RESULTS AND DISCUSSIONS

### 3.1 | Temperature-dependent Raman measurements in pristine regions

We have performed temperature-dependent Raman measurements within a pristine region of the investigated  $\text{KNbO}_3$  single-crystal sample to determine crystallographic phase transitions (see Figure 2). The sample was first cooled to 150 K and then gradually heated to 525 K.

At low temperatures, the Raman spectra can be assigned to the rhombohedral phase  $R3m$  of  $\text{KNbO}_3$ .<sup>23,50,51</sup> After a gradual increase in temperature, at 250 K new peaks appear at 273, 283, and  $608 \text{ cm}^{-1}$ , while the Raman mode at  $220 \text{ cm}^{-1}$  disappears, as shown in Figure 2. This change is related to a structural phase transition and results from the sensitivity of Raman spectroscopy to lattice dynamics. These Raman spectra can be assigned to the orthorhombic  $Amm2$  phase.<sup>23,50,51</sup> A broadening and shifting of the Raman modes occurs at elevated temperatures, which is

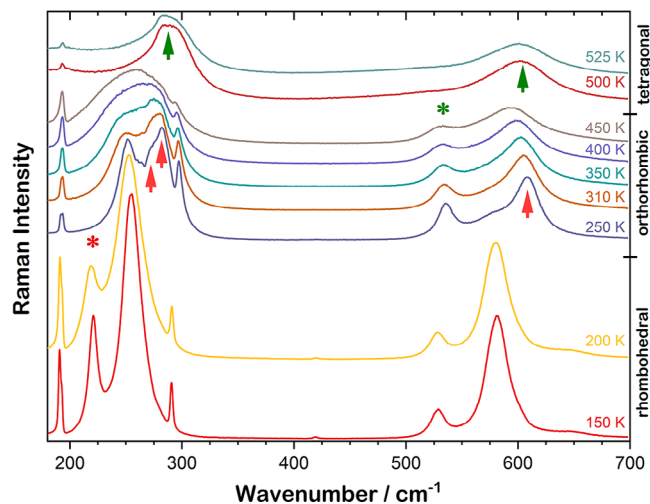


**FIGURE 2** Temperature-dependence of the Raman spectra in the range of 150–525 K. Structural phase transitions can be identified at 250 and 500 K due to the changes in Raman spectra. New Raman modes appear, which are indicated with arrows, while disappearing modes are marked with \*.

due to the thermal behavior of the phonons. Starting with 500 K, the appearance of broad Raman bands around  $300\text{ cm}^{-1}$  and vanishing of a mode around  $520\text{ cm}^{-1}$  can be observed. These changes indicate another phase transition whereby the new Raman spectra can be assigned to the tetragonal  $P4\text{ mm}$  phase of  $\text{KNbO}_3$  as expected from the literature.<sup>23,50,51</sup> The transition to the non-ferroelectric cubic phase at  $700\text{ K}$ <sup>23,50,51</sup> could not be observed due to the temperature limitation of the heating stage used.

We observed a thermal hysteresis during the low-temperature phase transition from rhombohedral to orthorhombic  $\text{KNbO}_3$ . This can be followed from the temperature evolution of the Raman peak at around  $295\text{ cm}^{-1}$ , as shown in Figure 3, which can be observed in both Raman spectra of each phase. The different peak positions in the rhombohedral and orthorhombic phases can be used to determine the phase transition temperature. There are differences in transition temperatures during heating and cooling process which can be attributed to a hysteresis and a first-order phase transition, which has already been discussed in the literature.<sup>24,52,53</sup>

## 3.2 | Dislocation-rich plastic zones

### 3.2.1 | Plastic zones and dislocation imaging

The dislocation-imprinted scratch tracks by the Brinell indenter scratching method can be seen in the polarized optical microscope image of Figure 4A for one (1 $\times$ ) and five (5 $\times$ ) Brinell passes. One pass (1 $\times$ ) is defined as a single gliding of the indenter on the sample surface in one

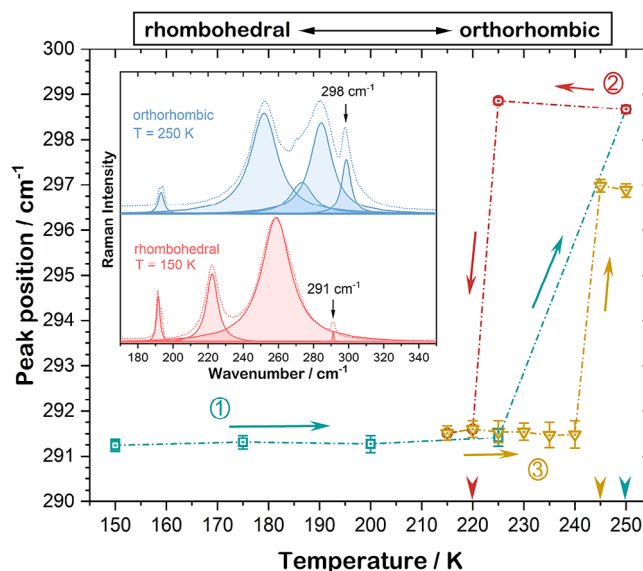


**FIGURE 3** The peak position of the Raman mode located at around  $295\text{ cm}^{-1}$  as a function of temperature during the rhombohedral–orthorhombic phase transition. The peak position was determined by fitting the Raman mode with Lorentz line shapes, as depicted in the inset. Thus, an abrupt shift in the peak position at a certain temperature acts as an indicator for the phase transition. The hysteresis can be seen by the different transition temperatures during heating (1 and 3) and cooling (2) which are marked in the figure (it should be noted that the measured temperatures in steps 1 to 3 are not the same).

direction from one end to the other end. These areas will be referred to as ‘Brinell zones’ in the following, in contrast to the reference pristine region. The plastically deformed Brinell zones can be distinguished from the pristine areas in the microscopic image (Figure 4A) by the presence of vertical and diagonal lines within them. These slip traces are caused by the interaction of the activated glide planes of the  $\langle 110 \rangle \{110\}$  slip system with the tested (100) surface of the sample, as illustrated in Figure 4B. The number of the slip traces increases with the number of Brinell passes, indicating higher dislocation densities.<sup>12</sup>

For visualizing dislocations, ECCI is a suitable technique.<sup>7,15,17</sup> Figure 5 demonstrates two images of the Brinell zones with one (1 $\times$ ) and ten (10 $\times$ ) Brinell passes, respectively. The bright dots are intersection points of dislocation lines with the (100) surface. Some of them are marked with arrows for better visibility.

### 3.2.2 | Raman measurements in the Brinell zone with one scratch pass

We performed a Raman line scan across the boundary between the 1 $\times$  Brinell zone and the pristine region outside at RT (see inset image in Figure 6A). This Brinell

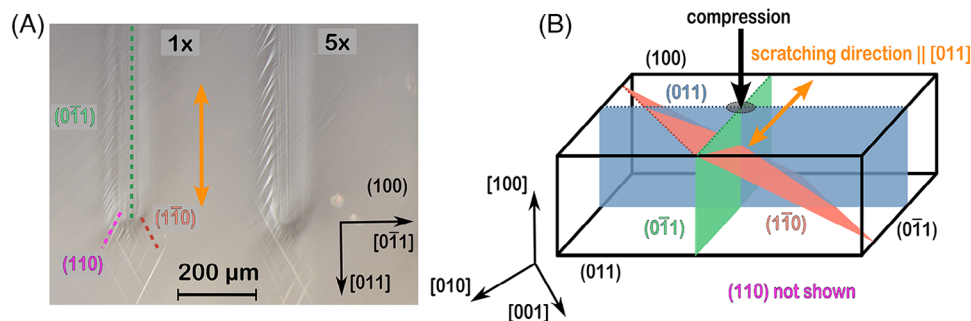


**FIGURE 4** (A) Polarized optical microscope image of deformed Brinell zones with one (1x) and five (5x) scratching repetitions. The intersection lines of the slip planes with the surface are indicated by dashed lines. (B) Schematic of the sample geometry and the activated slip planes during the deformation of the (100) surface by the Brinell indenter. All crystallographic directions correspond to the pseudo-cubic representation of the orthorhombic cell.

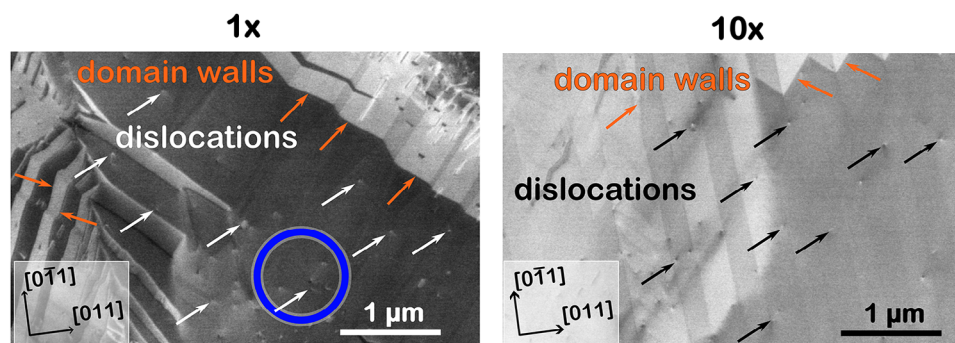


**FIGURE 5** ECCI of Brinell zones with 1x and 10x scratch passes. Selected dislocations are highlighted by arrows. The domain walls exhibit a striking zig-zag pattern, which was confirmed by piezo-response force microscopy measurements (see Figure S4b) and also been described by Preuß et al.<sup>15</sup> This is related to a dislocation-induced domain wall pinning effect.<sup>19</sup> The laser spot dimension (blue circle) is also marked to scale to illustrate the proportions of the investigated sample area. ECCI, Electron channelling contrast imaging.

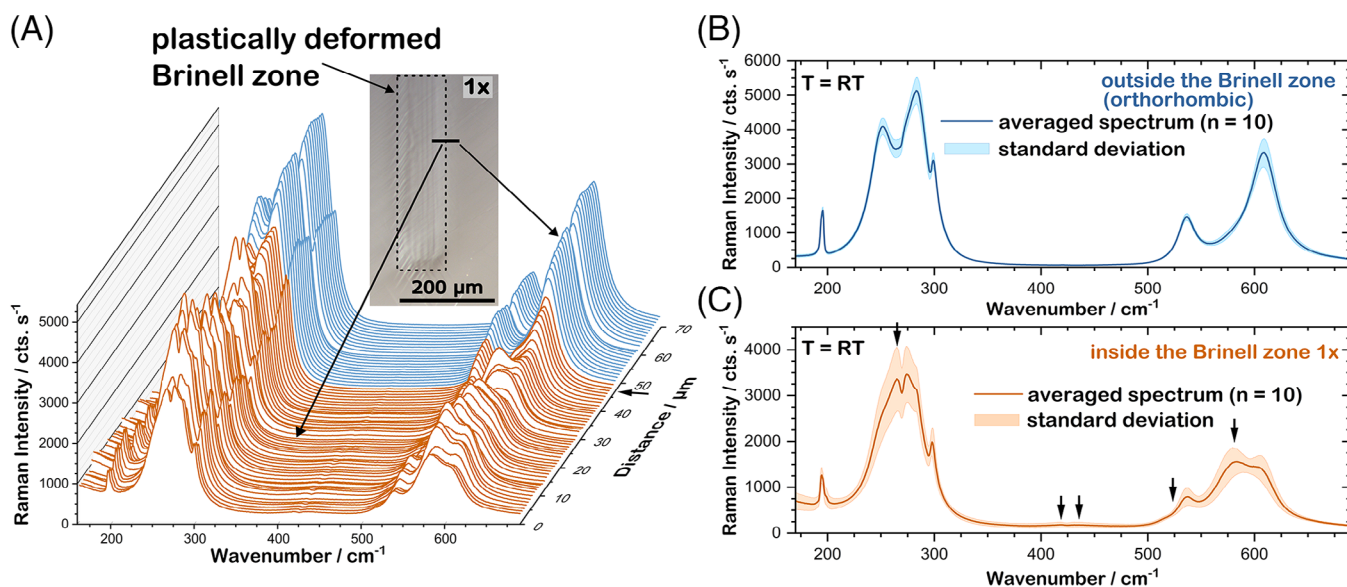


**FIGURE 6** (A) The Raman spectra correspond to the line scan across the boundary between the 1x Brinell zone and pristine region. (B,C) Averaged Raman spectrum of the region outside and inside the Brinell zone, respectively, obtained from the statistical average of 10 randomly selected Raman spectra from the corresponding regions. The range of the standard deviation is also shown. New Raman modes are observed in (C), which are highlighted with arrows.

zone will serve as a reference for our Raman studies in dislocation-rich regions. The Raman line scan in Figure 6A reveals changes in the Raman spectra during mapping. Using the positional information from the line scan and the optical microscope image, it is possible to assign the spectra to the respective sample region. Please note that the absolute measured intensities of the Raman signal in the deformed zone strongly depend on the position of the laser spot on the sample. This could be due to slip traces causing a step-like roughening of the surface. Such a surface in deformed  $\text{KNbO}_3$  was observed by Höfling et al.<sup>7</sup> using the atomic force microscopy (AFM). They obtained height differences in the range of several hundred nanometres. This affects the intensity of the measured Raman spectra, as the laser focus changes. To counteract this influence, an averaged spectrum was calculated from the mean value of the Raman intensities of 10 randomly selected spectra from this zone, which is presented in Figure 6C. This spectrum represents the entire Brinell zone and averages the intensity fluctuations of the individual spectra. For the sake of completeness, the same procedure was carried out for the area outside the Brinell zone (see Figure 6B). This spectrum can be assigned to the orthorhombic phase of the  $\text{KNbO}_3$ , which is consistent with the expected crystal structure at RT based on the temperature-dependent Raman measurements before (Figure 2) and results of DFT-calculations. According to space group  $Amm2$  there will be 12 vibrational modes for  $\text{KNbO}_3$  with irreducible representations  $4A_1 + A_2 + 4B_1 + 3B_2$ .<sup>23</sup> All modes are allowed to be Raman active due to the symmetry. The calculated phonon frequencies are listed in Table 1.

In contrast, in the plastically deformed Brinell zone, changes in the Raman spectrum can be observed (Figure 6C). Surprisingly, this Raman spectrum cannot be assigned to any known phase of  $\text{KNbO}_3$  (compare to Section 3.1) and is not described in the literature with such an appearance.<sup>23,24,52,53</sup> To determine the positions of the phonon modes, this new Raman spectrum was fitted with Lorentz oscillators, whose positions are represented in Table 1. Figure 7 displays the fit to the Raman signals. It can be seen that some Raman modes of the orthorhombic phase still appear in this spectrum when compared to the spectrum of the pristine region. Further, there are new Raman modes at 263, 418, 435, 522, and 581  $\text{cm}^{-1}$ , which only appear in the Brinell zone. In addition, there is a strong spectral background at low wavenumbers  $< 200 \text{ cm}^{-1}$  (see Figure 6C). This could be related to an increase in elastic scattering due to the changes in surface morphology.

In order to account for high dislocation densities, we assume that high defect concentrations may locally lower the crystal symmetry. For this reason, in the DFT calcula-

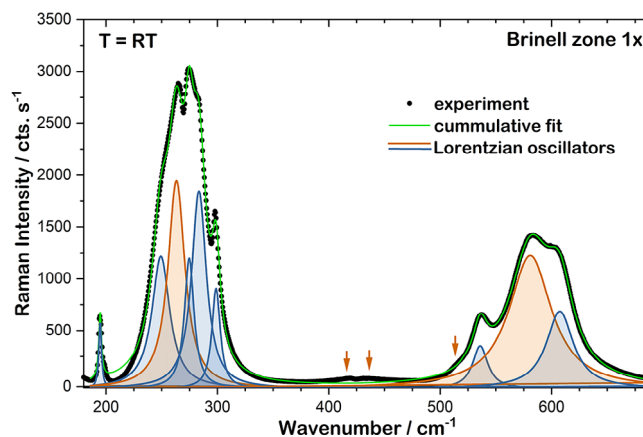


**FIGURE 7** The averaged and baseline-corrected Raman spectrum of the 1× Brinell zone is fitted with Lorentz oscillators. A distinction is made between Raman signals that can also be found in the pristine, orthorhombic areas (blue) of the sample and those that only occur in the plastically deformed Brinell zone (orange). The arrows mark the peak positions of very weak signals at 418, 435, and 522  $\text{cm}^{-1}$ , which also only occur in the Brinell zone.

tions, we set up a supercell using a simple orthorhombic cell containing two formula units  $\text{KNbO}_3$ , not using the fractional translation  $(0, 1/2, 1/2)$  available in space group  $Amm2$ , but treating the atoms as independent. This increases the number of atoms to 10 in that orthorhombic structure. Similar to the previous calculations, we relax the cell volume and atomic positions before calculating the vibrational frequencies. In that model structure due to the 10 independent atoms, we will get now 27 vibrational modes as shown in Table S1. The surprising observation is that this lowering of symmetry and small deviations of the atoms from ideal positions is enough to produce modes deviating in frequency from the full symmetric structure in space group  $Amm2$ . In particular, there are now new modes between 303 and 472  $\text{cm}^{-1}$ . We performed azimuthal angle-dependent Raman measurements in the pristine region (see Figure S1) and in the 1× Brinell zone (see Figure S2), as described in Supporting information. In contrast to the measurements in pristine  $\text{KNbO}_3$ , the Raman spectra recorded in the Brinell zone show a random angular dependence, which could be an indication of a symmetry loss in the crystal lattice caused by dislocations. This could confirm the previously discussed results of DFT calculations.

Surprisingly, such dislocation-induced activation of Raman modes is not observed in the low-temperature rhombohedral phase of  $\text{KNbO}_3$ . The Raman spectra recorded in the pristine and 1× Brinell zone do not show any differences, as presented in Figure S3. Both can be assigned to the rhombohedral phase (see Section 3.1). Despite the similarities, we suppose that the dislocations

**TABLE 1** The observed Raman mode frequencies of plastically deformed KNbO<sub>3</sub> (Brinell zone 1×) in comparison with orthorhombic KNbO<sub>3</sub> (DFT-calculated and Ref. [53]).

Wavenumber (cm <sup>-1</sup> ) Brinell zone 1× (experiment)	Wavenumber (cm <sup>-1</sup> ) orthorhombic ( <i>Amm</i> 2) (DFT-calculated)	Assignment (DFT-calculated)	Wavenumber (cm <sup>-1</sup> ) orth. KNbO <sub>3</sub> (Ref. [53]) (experiment)	Assignment (Ref. [53])
	46.2	B <sub>2</sub>		
	169.1	A <sub>1</sub>		
	172.2	B <sub>2</sub>		
	173.1	B <sub>1</sub>		
			192	B <sub>1</sub> (TO)
			193	A <sub>1</sub> (TO)
195			194.5	A <sub>1</sub> (LO)
249	246.3	B <sub>1</sub>	249	B <sub>1</sub> (TO)
263*				
274			270	B <sub>1</sub> (TO)
			281.5	A <sub>1</sub> (TO)
283	271.2	A <sub>2</sub>	282	A <sub>2</sub>
	283.7	B <sub>1</sub>		
	285.1	A <sub>1</sub>	295	A <sub>1</sub> (LO)
298			297	A <sub>1</sub> (TO)
418*				
435*	303.6	A <sub>1</sub>	434.5	A <sub>1</sub> (LO)
	472.7	B <sub>2</sub>	513	B <sub>2</sub> (TO)
522*				
535	527.7	B <sub>1</sub>	534	B <sub>1</sub> (TO)
581*				
607	601.5	A <sub>1</sub>	606.5	A <sub>1</sub> (TO)

Note: The Raman signals marked with \* only occur in the Brinell zones, not in the pristine region (resp. orthorhombic KNbO<sub>3</sub>).

are still preserved in the plastic region at low temperatures, since the above-mentioned differences in the Raman spectra reappear after reheating and transition back to the orthorhombic phase (see Figure S3). However, these Raman signals could have a symmetry-caused lower excitation probability, resulting in smaller signal intensities which are superimposed by more intense Raman signals from pristine rhombohedral regions between the dislocations.

### 3.2.3 | Raman measurements in Brinell zones with multiple scratch passes

The number of Brinell passes correlates with the imprinted dislocation density in single-crystal KNbO<sub>3</sub>, as has been experimental visualized by Preuß et al.<sup>15</sup> The dislocation density increases with increasing number of passes, from  $\sim 2 \times 10^{11} \text{ m}^{-2}$  in the pristine region to  $\sim 4 \times 10^{13} \text{ m}^{-2}$  after ten scratch passes where saturation occurs.<sup>15</sup>

Here, we further analyze and compare the Raman spectra in the Brinell zones with five (5×) and ten (10×)

scratch passes with the previously described 1× zone. Raman line scans were performed within the plastically deformed regions. As explained in Section 3.2.2, an averaged spectrum was calculated for each Brinell zone from 10 randomly selected Raman spectra. Figure 8A illustrates the averaged Raman spectra of the 5× and 10× Brinell zones together with the averaged spectrum of the 1× zone from Section 3.2.2. The number of observed Raman modes is the same in all three cases. Changes in the number of passes did not lead to new Raman signals. However, a change in peak positions can be observed in Figure 8B for three selected modes. These shift to higher peak positions as the number of passes increases (hence higher dislocation densities). Such a blueshift of the Raman peak position is present in strained crystals with compressive stresses.<sup>27</sup> Due to the spatial resolution limit of micro-Raman spectroscopy, the observed stress field does not originate from individual dislocations. Rather, it is an accumulated stress field resulting from the collective behavior of the dislocations after indentation. They form a geometric order that results in a residual compressive stress field. Similar Raman spectroscopic observations can be found in

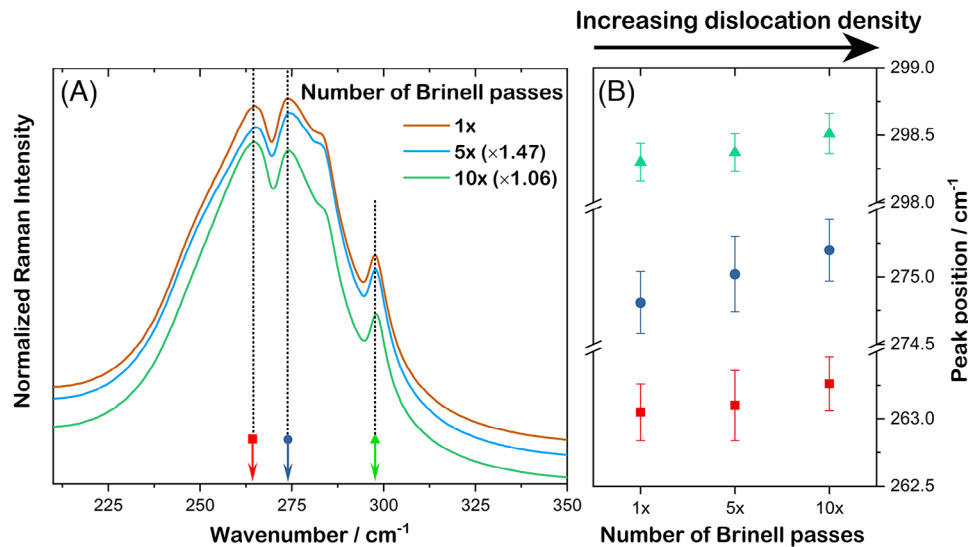


**FIGURE 8** (A) Averaged and normalized Raman spectra of the Brinell zones with different scratch passes. The scaling factors are given in the legend. (B) Peak positions of three selected Raman modes as a function of the number of scratch passes, determined by fitting them to Lorentzian line shapes. The blueshift indicates an increase in compressive strain with increasing Brinell passes.

the literature for various materials.<sup>32–35</sup> It would be very interesting to understand the relation between dislocation-induced stresses and Raman spectroscopy in more detail in future studies.

#### 4 | CONCLUSION

We use Raman spectroscopy to provide in-depth information on dislocation induced changes of local crystal order in single-crystal  $\text{KNbO}_3$ . charge-coupled device Temperature-dependent Raman measurements between 150 and 525 K in pristine  $\text{KNbO}_3$  reveal transitions among three phases, namely, at 250 K from the rhombohedral to the orthorhombic phase and at 500 K from the orthorhombic to the tetragonal phase. A thermal hysteresis is observed at the rhombohedral–orthorhombic phase transition, confirming the first-order phase transition behavior. Dislocation-rich regions were introduced by plastic deformation using the cyclic Brinell indenter scratching method. Contrasting the pristine regions, room-temperature Raman spectra reveal new Raman modes in dislocation-rich regions, which is likely caused by the high defect density that can lead to a reduction in the crystal symmetry (hence increased disorder), as confirmed by the azimuthal angle-dependent Raman measurements. The experimental results are supported by DFT calculations that yield 27 Raman-active modes in the dislocation-rich  $\text{KNbO}_3$ . This is a significant increase in the number of vibrational modes compared to the pristine orthorhombic structure, where 12 Raman active modes are expected due

to the symmetry. Furthermore, the increase in dislocation densities by increasing the number of scratch passes from 1 to 10 do not alter the Raman modes but lead to an increase in local compressive stresses, as evidenced by the blueshift of peak positions in the Raman spectra of regions with different dislocation densities. This is related to the collective behavior of the dislocations, resulting in an accumulated stress field due to a geometrically ordered dislocation structure. Our work contributes to the development of dislocation-tuned ceramics by understanding the changes in the crystal structure and associated dislocation dynamics. The relationship between Raman spectroscopy and dislocation-induced stresses and crystal symmetry lowering requires further investigation.

#### ACKNOWLEDGMENTS

F.D. thanks for the financial support by the Deutsche Forschungsgemeinschaft (DFG, German Research Foundation)—project number: 461482547. O.P. acknowledges the financial support by the Deutsche Forschungsgemeinschaft—project number: 414179371. X.F. acknowledges the financial support by the European Research Council (ERC) under Grant number: 101076167 (MECERDIS) for supporting the research. We thank Prof. Jens Götze at Institute for Mineralogy at TU Bergakademie Freiberg for the polarization microscope measurements. We further thank Dr. Enrico Bruder at TU Darmstadt for performing the ECCI imaging and Dr. Fangping Zhuo at TU Darmstadt for assisting with the PFM measurements.

Open access funding enabled and organized by Projekt DEAL.

## ORCID

Felix Drechsler  <https://orcid.org/0009-0004-9030-9104>

Cameliu Himcinschi  <https://orcid.org/0000-0002-5572-0393>

Xufei Fang  <https://orcid.org/0000-0002-3887-0111>

Jens Kortus  <https://orcid.org/0000-0001-9351-7022>

## REFERENCES

- Huang H, Scott JF, editors. Ferroelectric materials for energy applications. 1st ed. Weinheim: Wiley-VCH Verlag GmbH & Co. KGaA; 2018.
- Xu Y. Ferroelectric materials and their applications. Amsterdam, NY: North-Holland. Sole distributors for the USA and Canada. Elsevier Science Pub. Co; 1991.
- Zhang S, Malić B, Li J-F, Rödel J. Lead-free ferroelectric materials: prospective applications. *J Mater Res*. 2021;36(5):985–95. <https://doi.org/10.1557/s43578-021-00180-y>
- Yao Z, Liu H, Cao M, Hao H, Yu Z. Effects of Mn doping on the structure and electrical properties of high-temperature BiScO<sub>3</sub>–PbTiO<sub>3</sub>–Pb(Zn<sub>1/3</sub>Nb<sub>2/3</sub>)O<sub>3</sub> piezoelectric ceramics. *Mater Res Bull*. 2011;46(8):1257–61. <https://doi.org/10.1016/j.materresbull.2011.03.034>
- Hreščak J, Dražić G, Deluca M, Arčon I, Kodre A, Dapiaggi M, et al. Donor doping of K<sub>0.5</sub>Na<sub>0.5</sub>NbO<sub>3</sub> ceramics with strontium and its implications to grain size, phase composition and crystal structure. *J Eur Ceram Soc*. 2017;37(5):2073–82. <https://doi.org/10.1016/j.jeurceramsoc.2016.12.053>
- Maarouf AA, Gogova D, Fadlallah MM. Metal-doped KNbO<sub>3</sub> for visible light photocatalytic water splitting: a first principles investigation. *Appl Phys Lett*. 2021;119(6):063901. <https://doi.org/10.1063/5.0058065>
- Höfling M, Trapp M, Porz L, Uršič H, Bruder E, Kleebe H-J, et al. Large plastic deformability of bulk ferroelectric KNbO<sub>3</sub> single crystals. *J Eur Ceram Soc*. 2021;41(7):4098–107. <https://doi.org/10.1016/j.jeurceramsoc.2021.02.023>
- Brunner D, Taeri-Baghadrani S, Sigle W, Rühle M. Surprising results of a study on the plasticity in strontium titanate. *J Am Ceram Soc*. 2001;84(5):1161–63. <https://doi.org/10.1111/j.1151-2916.2001.tb00805.x>
- Yang K-H, Ho N-J, Lu H-Y. Plastic deformation of <001> single-crystal SrTiO<sub>3</sub> by compression at room temperature. *J Am Ceram Soc*. 2011;94(9):3104–11. <https://doi.org/10.1111/j.1551-2916.2011.04473.x>
- Fang X, Zhang J, Frisch A, Preuß O, Okafor C, Setvin M, et al. Room-temperature bulk plasticity and tunable dislocation densities in KTaO<sub>3</sub>. *J Am Ceram Soc*. 2024;107(11):7019–643. <https://doi.org/10.1111/jace.20040>
- Fang X. Mechanical tailoring of dislocations in ceramics at room temperature: A perspective. *J Am Ceram Soc*. 2024;107(3):1425–47. <https://doi.org/10.1111/jace.19362>
- Fang X, Preuß O, Breckner P, Zhang J, Lu W. Engineering dislocation-rich plastic zones in ceramics via room-temperature scratching. *J Am Ceram Soc*. 2023;106(8):4540–45. <https://doi.org/10.1111/jace.20040>
- Okafor C, Ding K, Zhou X, Durst K, Rödel J, Fang X. Mechanical tailoring of dislocation densities in SrTiO<sub>3</sub> at room temperature. *J Am Ceram Soc*. 2022;105(4):2399–402. <https://doi.org/10.1111/jace.18277>
- Fang X, Nakamura A, Rödel J. Deform to perform: dislocation-tuned properties of ceramics. *Am Ceram Soc Bull*. 2023;102:24–29.
- Preuß O, Bruder E, Lu W, Zhuo F, Minnert C, Zhang J, et al. Dislocation toughening in single-crystal KNbO<sub>3</sub>. *J Am Ceram Soc*. 2023;106(7):4371–81. <https://doi.org/10.1111/jace.19088>
- Johanning M, Porz L, Dong J, Nakamura A, Li J-F, Rödel J. Influence of dislocations on thermal conductivity of strontium titanate. *Appl Phys Lett*. 2020;117(2):021902. <https://doi.org/10.1063/5.0010234>
- Szot K, Rodenbücher C, Bihlmayer G, Speier W, Ishikawa R, Shibata N, et al. Influence of dislocations in transition metal oxides on selected physical and chemical properties. *Crystals*. 2018;8(6):241. <https://doi.org/10.3390/cryst8060241>
- Porz L, Klomp AJ, Fang X, Li N, Yildirim C, Detlefs C, et al. Dislocation-toughened ceramics. *Mater Horiz*. 2021;8(5):1528–37. <https://doi.org/10.1039/d0mh02033h>
- Höfling M, Zhou X, Riemer LM, Bruder E, Liu B, Zhou L, et al. Control of polarization in bulk ferroelectrics by mechanical dislocation imprint. *Science*. 2021;372(6545):961–64. <https://doi.org/10.1126/science.abe3810>
- Zhuo F, Zhou X, Gao S, Höfling M, Dietrich F, Groszewicz PB, et al. Anisotropic dislocation-domain wall interactions in ferroelectrics. *Nat Commun*. 2022;13(1):6676. <https://doi.org/10.1038/s41467-022-34304-7>
- Zhou X, Liu Z, Xu B-X. Influence of dislocations on domain walls in perovskite ferroelectrics: phase-field simulation and driving force calculation. *Int J Solids Struct*. 2022;238:111391. <https://doi.org/10.1016/j.ijsolstr.2021.111391>
- Himcinschi C, Drechsler F, Walch DS, Bhatnagar A, Belik AA, Kortus J. Unexpected phonon behaviour in BiFe<sub>x</sub>Cr<sub>1-x</sub>O<sub>3</sub>, a material system different from its BiFeO<sub>3</sub> and BiCrO<sub>3</sub> parents. *Nanomaterials*. 2022;12(9):1607. <https://doi.org/10.3390/nano12091607>
- Baier-Saip JA, Ramos-Moor E, Cabrera AL. Raman study of phase transitions in KNbO<sub>3</sub>. *Solid State Commun*. 2005;135(6):367–72. <https://doi.org/10.1016/j.ssc.2005.05.021>
- Fontana MP, Razzetti C. Raman spectroscopy of the orthorhombic–rhombohedral structural transition in ferroelectric KNbO<sub>3</sub>. *Solid State Commun*. 1975;17(3):377–80. [https://doi.org/10.1016/0038-1098\(75\)90315-4](https://doi.org/10.1016/0038-1098(75)90315-4)
- Himcinschi C, Vrejoiu I, Weißbach T, Vijayanandhini K, Talkenberger A, Röder C, et al. Raman spectra and dielectric function of BiCrO<sub>3</sub>: experimental and first-principles studies. *J Appl Phys*. 2011;110(7):073501. <https://doi.org/10.1063/1.3642985>
- Himcinschi C, Guo E-J, Talkenberger A, Dörr K, Kortus J. Influence of piezoelectric strain on the Raman spectra of BiFeO<sub>3</sub> films deposited on PMN-PT substrates. *Appl Phys Lett*. 2016;108(4):042902. <https://doi.org/10.1063/1.4940973>
- Himcinschi C, Vrejoiu I, Friedrich M, Nikulina E, Ding L, Cobet C, et al. Substrate influence on the optical and structural properties of pulsed laser deposited BiFeO<sub>3</sub> epitaxial films. *J Appl Phys*. 2010;107(12):091110. <https://doi.org/10.1063/1.3437059>
- Dobrosz P, Bull SJ, Olsen SH, O'Neill AG. The use of Raman spectroscopy to identify strain and strain relaxation in strained Si/SiGe structures. *Surf Coat Technol*. 2005;200(5-6):1755–60. <https://doi.org/10.1016/j.surfcoat.2005.08.048>
- Himcinschi C, Rix J, Röder C, Rudolph M, Yang M-M, Rafaja D, et al. Ferroelastic domain identification in BiFeO<sub>3</sub> crystals using

- Raman spectroscopy. *Sci Rep.* 2019;9(1):379. <https://doi.org/10.1038/s41598-018-36462-5>
30. Seo J, Nahm H-H, Park H-S, Yun S, Lee JH, Kim Y-J, et al. Detection of the prototype symmetry of ferroelastic WO<sub>3</sub> domain walls by angle-resolved polarized Raman spectroscopy. *Phys Rev B.* 2023;108(1):014103. <https://doi.org/10.1103/PhysRevB.108.014103>
  31. Irmer G, Jurisch M. Micro-Raman study of strain fields around dislocations in GaAs. *Phys Status Solidi a.* 2007;204(7):2309–18. <https://doi.org/10.1002/pssa.200723041>
  32. Nootz G, Schulte A, Chernyak L, Osinsky A, Jasinski J, Benamara M, et al. Correlations between spatially resolved Raman shifts and dislocation density in GaN films. *Appl Phys Lett.* 2002;80(8):1355–57. <https://doi.org/10.1063/1.1449523>
  33. Lei H, Leipner HS, Schreiber J, Weyher JL, Wosiński T, Grzegory I. Raman and cathodoluminescence study of dislocations in GaN. *J Appl Phys.* 2002;92(11):6666–70. <https://doi.org/10.1063/1.1518793>
  34. Wermelinger T, Borgia C, Solenthaler C, Spolenak R. 3-D Raman spectroscopy measurements of the symmetry of residual stress fields in plastically deformed sapphire crystals. *Acta Mater.* 2007;55(14):4657–65. <https://doi.org/10.1016/j.actamat.2007.04.036>
  35. Wermelinger T, Spolenak R. Symmetry of residual stress fields of ZnO below an indent measured by three-dimensional Raman spectroscopy. *J Appl Phys.* 2009;106(6):064907. <https://doi.org/10.1063/1.3224891>
  36. Khayr I, Hameed S, Budić J, He X, Spieker R, Najev A, et al. Structural properties of plastically deformed SrTiO<sub>3</sub> and KTaO<sub>3</sub>. *arXiv.* 2024. <https://doi.org/10.48550/arXiv.2405.13249>
  37. Hameed S, Pelc D, Anderson ZW, Klein A, Spieker RJ, Yue L, et al. Enhanced superconductivity and ferroelectric quantum criticality in plastically deformed strontium titanate. *Nat Mater.* 2022;21(1):54–61. <https://doi.org/10.1038/s41563-021-01102-3>
  38. Götze J. Application of Nomarski DIC and cathodoluminescence (CL) microscopy to building materials. *Mater Charact.* 2009;60(7):594–602. <https://doi.org/10.1016/j.matchar.2008.09.006>
  39. Zaefferer S, Elhami N-N. Theory and application of electron channelling contrast imaging under controlled diffraction conditions. *Acta Mater.* 2014;75:20–50. <https://doi.org/10.1016/j.actamat.2014.04.018>
  40. Medrano C, Voit E, Amrhein P, Günter P. Optimization of the photorefractive properties of KNbO<sub>3</sub> crystals. *J Appl Phys.* 1988;64(9):4668–73. <https://doi.org/10.1063/1.341249>
  41. Brehm S, Himcinschi C, Kraus J, Kortus J. PyRamanGUI: open-source graphical user interface for analyzing Raman spectra. *SoftwareX.* 2023;23:101486. <https://doi.org/10.1016/j.softx.2023.101486>
  42. Hohenberg P, Kohn W. Inhomogeneous electron gas. *Phys Rev.* 1964;136(3B):B864–71. <https://doi.org/10.1103/PhysRev.136.B864>
  43. Kohn W, Sham LJ. Self-consistent equations including exchange and correlation effects. *Phys Rev.* 1965;140(4A):A1133–38. <https://doi.org/10.1103/PhysRev.140.A1133>
  44. Giannozzi P, Baroni S, Bonini N, Calandra M, Car R, Cavazzoni C, et al. QUANTUM ESPRESSO: a modular and open-source software project for quantum simulations of materials. *J Phys Condens Matter.* 2009;21(39):395502. <https://doi.org/10.1088/0953-8984/21/39/395502>
  45. Giannozzi P, Andreussi O, Brumme T, Bunau O, Buongiorno Nardelli M, Calandra M, et al. Advanced capabilities for materials modelling with Quantum ESPRESSO. *J Phys Condens Matter.* 2017;29(46):465901. <https://doi.org/10.1088/1361-648X/aa8f79>
  46. Giannozzi P, Baseggio O, Bonfà P, Brunato D, Car R, Carnimeo I, et al. Quantum ESPRESSO toward the exascale. *J Chem Phys.* 2020;152(15):154105. <https://doi.org/10.1063/5.0005082>
  47. Blöchl PE. Projector augmented-wave method. *Phys Rev B: Condens Matter.* 1994;50(24):17953–79. <https://doi.org/10.1103/physrevb.50.17953>
  48. Dal Corso A. Pseudopotentials periodic table: From H to Pu. *Comput Mater Sci.* 2014;95:337–50. <https://doi.org/10.1016/j.commatsci.2014.07.043>
  49. Perdew JP, Burke K, Ernzerhof M. Generalized gradient approximation made simple. *Phys Rev Lett.* 1996;77(18):3865–68. <https://doi.org/10.1103/PhysRevLett.77.3865>
  50. Fontana MD, Metrat G, Servoin JL, Gervais F. Infrared spectroscopy in KNbO<sub>3</sub> through the successive ferroelectric phase transitions. *J Phys C: Solid State Phys.* 1984;17(3):483–514. <https://doi.org/10.1088/0022-3719/17/3/020>
  51. Hewat AW. Cubic-tetragonal-orthorhombic-rhombohedral ferroelectric transitions in perovskite potassium niobate: neutron powder profile refinement of the structures. *J Phys C: Solid State Phys.* 1973;6(16):2559–72. <https://doi.org/10.1088/0022-3719/6/16/010>
  52. Baier-Saip JA, Gutierrez MH, Cabrera AL, Baier PA. Hysteresis in the rhombohedral–orthorhombic phase transition of KNbO<sub>3</sub> under inhomogeneous strain. *Solid State Commun.* 2013;154:6–10. <https://doi.org/10.1016/j.ssc.2012.10.029>
  53. Quittet AM, Bell MI, Krauzman M, Raccah PM. Anomalous scattering and asymmetrical line shapes in Raman spectra of orthorhombic KNbO<sub>3</sub>. *Phys Rev B.* 1976;14(11):5068–72. <https://doi.org/10.1103/PhysRevB.14.5068>

## SUPPORTING INFORMATION

Additional supporting information can be found online in the Supporting Information section at the end of this article.

**How to cite this article:** Drechsler F, Himcinschi C, Preuß O, Fang X, Kortus J. Dislocation-induced local symmetry reduction in single-crystal KNbO<sub>3</sub> observed by Raman spectroscopy. *J Am Ceram Soc.* 2024;e20221. <https://doi.org/10.1111/jace.20221>